M. Bender, G. B. Olson, ICOMAT '08, June 2008.

DESIGNING A PRECIPITATION-STRENGTHENED, SUPERELASTIC, TINI-BASED ALLOY FOR ENDOVASCULAR STENTS

Matthew D. Bender, Gregory B. Olson
Northwestern University; 2220 Campus Dr.; Evanston, IL 60208, USA

Keywords: NiTi, TiNi, NiTiAl, NiPdTiAl, Heusler, stent, precipitation-strengthened, superelastic

Abstract

The design of a precipitation-strengthened, superelastic, biomedical alloy for the application of endovascular stenting demonstrates the effectiveness of models for aluminide precipitation-strengthening, transformation temperature, interphase misfit, and radiopacity. While earlier research focused on the role of zirconium in these alloys, current research quantifies the role of palladium. A newly designed $Ni_{20}Pd_{30}Ti_{46}Al_4$ (at.%) alloy that is superelastic at body temperature demonstrates greatly enhanced thermal and mechanical cyclic stability over binary TiNi.

Introduction

Nitinol alloys suffer from limited cyclic fatigue life, causing loss of superelasticity and even catastrophic failure. Compliant TiNi endovascular stents are subjected to severe fatigue conditions in the superficial femoral artery. Current material limitations in fatigue and strength require the design of a new class of nanoscale precipitation-strengthened shape-memory alloys that meet current and future material performance goals.

TiNi Cyclic Instability

TiNi shape-memory alloy is well known to suffer from instability during thermal and/or mechanical cycling. This cycling results in the formation and accumulation of slip dislocations, which reduces alloy superelasticity. Using TEM, Miyazaki *et al.* observed these slip dislocations in a solution treated $Ti_{51.2}Ni_{49.8}$ binary alloy that was thermally cycled up to 100 times, as shown in Figure 1 [1], and correlated an increase in dislocation density with a decrease in the measured M_s transformation temperature. Based on those observations, Miyazaki *et al.* conclude that the thermal cycling effect in TiNi alloys is attributed to the stress fields of accommodation slip dislocations introduced by transformation.

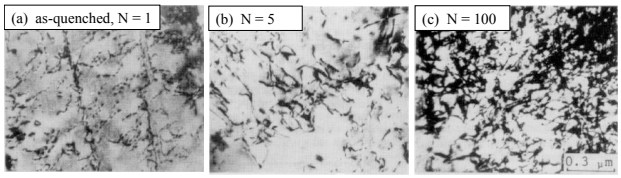

Figure 1. Increasing dislocation density with thermal cycling, as observed by Miyazaki *et al.* [1]

Olson and Owen [2] calculated the shear stress around a martensite plate in the Fe_3Pt system and demonstrated very large stresses close to the edge of the plate, as illustrated in Figure 2. When the maximum shear stress applied reaches the critical stress of the alloy, the plastic zone size can be computed as illustrated by Figure 3. In disordered material, there is a large plastic zone enclosing a volume several times larger than the martensite particle itself making elastic accommodation impossible. In ordered material, the plastic zone disappears entirely except at the periphery of the martensite plate.

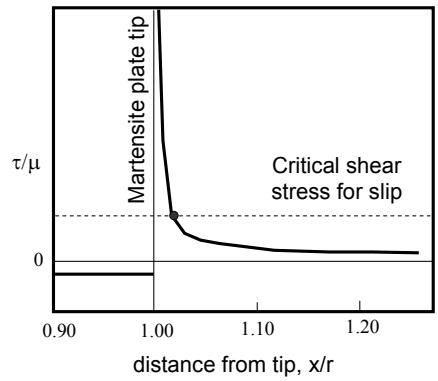

Figure 2. Illustration (from Olson and Owen [2]) of in-plane shear stress versus distance from martensite plate tip

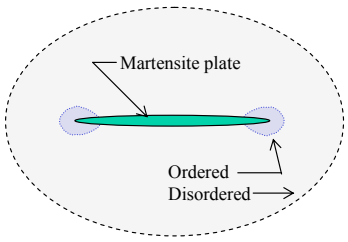

Figure 3. Illustration (from Olson and Owen [2]) of plastic zone contour around a martensite showing effect of order strengthening in Fe_3Pt

Increasing the flow stress of the B2 parent phase should decrease the cyclic instability of TiNi. The superelastic stress-strain results in Figure 4 (published by Adler *et al.* [3], first measured by Zadno *et al.* [4]) demonstrate this effect. As the parent B2 phase flow stress is increased from 737 MPa in a solution treated TiNi alloy to 1360 MPa in a cold-worked and aged TiNi alloy, the permanent strain is significantly decreased. Therefore, an increase in B2 parent phase strength should result in improved fatigue life.

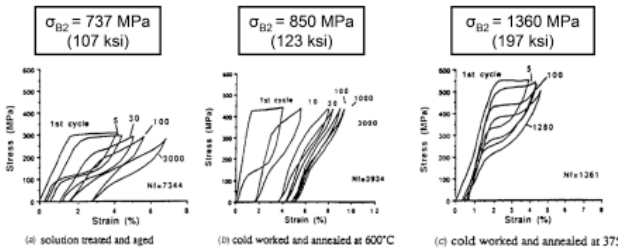

Figure 4. Reduction in TiNi instability as B2 strength increases [3,4]

Mechanical deformation processes are most often used to increase the yield strength of TiNi alloys. Introducing a dislocation substructure is not the most promising approach for increased fatigue life. Instead, a precipitation-strengthening approach using the addition of Al to TiNi forming the Ni_2TiAl $L2_1$ Heusler phase, as described and implemented by Jung *et al.* [5], is followed here. To avoid interphase misfit as a source of irreversibility through coherency loss during transformation, the misfit will be decreased by alloying large atoms that partition to and expand the $L2_1$ unit cell at 600°C.

Macroscopically, increasing the critical stress for slip will increase the output stress of the martensite to austenite transformation. Microscopically, austenite strengthening promotes reversible twinning and detwinning instead of irreversible plastic deformation caused by slip.

Endovascular Stent Fatigue

Atherosclerosis is a condition where plaque builds up in blood vessels, restricting blood flow as well as the exchange of nutrients, oxygen, waste, and gases between blood and body tissue. Angioplasty is a minimally invasive operation used to treat atherosclerosis, using a balloon catheter to compress the plaque and to restore proper blood flow. Stents are devices used to scaffold the inside circumference of a blood vessel following angioplasty, decreasing the propensity for restenosis, or a re-narrowing of the vessel. Superelastic TiNi stents are most often used to stent the superficial femoral artery and carotid artery because superelastic stents preserve the natural physiology of the body, allowing an artery to bend, crush, stretch, and twist. Another advantage is that TiNi stents do not interrupt blood flow during deployment.

Unfortunately, TiNi alloys are constrained in these applications by limited cyclic fatigue life causing loss of superelasticity. Although the U.S. Food and Drug Administration requires stents to have a fatigue life of 10 years, chronic overloads applied by the body in addition to pulsatile background loading often lead to premature failures. Experimental studies by Riepe *et al.* [6] and Allie *et al.* [7] both approximate a 30% failure rate of SFA stents. Allie *et al.* [7] claim an approximate 20% failure rate of TiNi SFA stents, which are characterized by fracture. Medical stent failure can cause restenosis, thrombosis, and even pseudoaneurysm. A superelastic medical alloy with much improved cyclic fatigue life is in high demand.

TiNi Alloys By Design

Recently, Bender and Olson studied the nanodispersion strengthening of Heusler $Ni_2(Ti,Zr)Al$ precipitates in NiTiZrAl alloys showing that the composition trajectory was consistent with Langer-Schwartz theory for precipitation at high supersaturation and could thus be modeled with unstable equilibrium conditions [8]. Their calibrated strengthening model of shear and Orowan strengthening regimes predicted an optimal particle diameter of 3.1 nm following a 10 hr aging treatment at 600°C leading to maximum alloy strengthening. Jung et al. previously determined the partitioning behavior of Zr, Hf, and Pd at 600°C, finding that all three elements partitioned favorably to the aluminide phase reducing $B2/L2_1$ interphase misfit [5]. Misfit elastic energy reduces the driving force for dispersion refinement and it can also make the dispersion unstable during transformation through loss of coherency.

A system structure diagram for (Ni,Pd,Pt)(Ti,Zr,Al) alloys detailing the processing-structure-properties-performance relationships is shown in Figure 5. The current study seeks to significantly improve the performance of superelastic TiNi-based medical alloys, specifically NiPdTiAl alloys. High strength, as demonstrated through the output stress, is desired. High fatigue resistance can be obtained through minimization of accommodation slip. It is important to maintain or improve biocompatibility with elemental substitution. The alloy must be superelastic at body temperature (37°C); corresponding to an austenite finish temperature of around 10-15°C. Finally, an optimized medical alloy should have higher radiopacity than current stent materials. Substitution of elements with higher atomic numbers increases the mass attenuation of an alloy, which increases x-ray absorption.

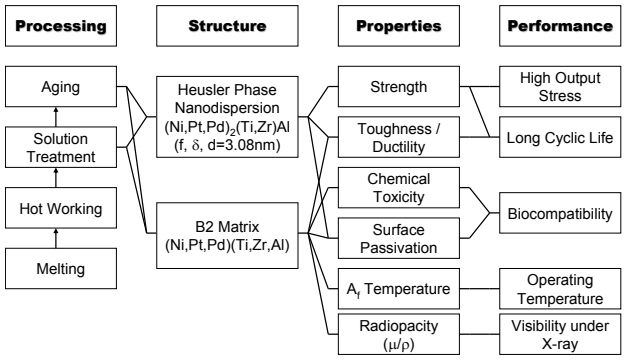

Figure 5. The system structure flow/block diagram for high-performance TiNi-based medical alloys

Ti is widely used in biomedical devices because it is biocompatible; however, Ni itself is toxic and carcinogenic. TiNi is generally safe due to a stable TiO_2 passivation layer that forms on TiNi and prevents Ni from leeching into the body. The biocompatibility of TiNi-based alloys can be maintained by not disrupting surface passivation and can be improved by substituting Ni with a less toxic element. While the toxicity of Al is debated in the literature and has been implicated in some disorders [9], it is currently used in biocompatible Ti6Al4V and thus is deemed safe to use in small amounts. The toxicity level of Zr is very low and Zr is not associated with adverse reactions in the body [10-13]. Pt is a highly corrosion resistant material and also is safe. The toxicity of Pd is relatively low and Pd is deemed safe as it is excreted rapidly from the body [9,14-16]. Thus, while Ni(Ti,Zr,Al) alloys should maintain biocompatibility, (Ni,Pd,Pt)(Ti,Zr,Al) alloys should improve biocompatibility.

Experimental

NiTiAl, NiPtTiZrAl, and NiPdTiAl alloys were prepared as 2-10 gram buttons by an arc-melting method. Each arc-melted button was re-melted five times to ensure complete mixing. The buttons were then encapsulated in quartz capsules under vacuum, solution treated at 950°C, and quenched by crushing the quartz capsules in oil. Aging was also performed in evacuated quartz capsules at 600°C.

Voltage-pulsed local electrode atom probe (LEAP) microanalysis, with a pulse rate of 200 kHz at 80 K, was utilized to study the Heusler phase nanodispersion and the partitioning behavior of Pt in the B2-$L2_1$ system at 600°C. Atom probe specimens were fabricated into needle shapes either by electropolishing or a dual-beam focused-ion beam milling technique.

Transformation temperatures were measured using a Perkins Differential Scanning Calorimeter (DSC) with a heating and cooling rate of 10°C/min. The transformation temperatures were estimated from the intersection between the baseline and the steepest slopes of the peak.

Mechanical compression testing was performed on a Sintech, model 20/G machine at a strain rate of 2.8×10^{4} s^{-1}. An Instron convection oven encompassed the text fixtures allowing testing up to 200°C. Compression cylinders were EDM machined from arc melted buttons. Loads were measured with a load cell while strains were measured by the crosshead displacement. The machine compliance was measured at test temperature and subtracted from the compression measurements. While superelasticity is better demonstrated in tension tests, the samples were tested in compression due to the limited specimen dimensions.

The x-ray fluoroscopy comparison study was performed at Northwestern Memorial Hospital using a Philips V-5000x x-ray fluoroscope. Samples were thinned to a 127 μm cross-section and compared to an Al wedge of varying thickness. Images were shot on a 15-inch field size with the shutters brought in on the lowest possible acquisition system. Images were obtained with a 60 kVp operating voltage and 204 ms.

A preliminary in-vitro cytology study was performed on the designed alloy to assess biocompatibility [17,18]. Ti, Ni, TiNi, and $Ni_{20}Pd_{30}Ti_{46}Al_4$ metal powders were obtained or prepared by grinding. Human coronary artery endothelial cells (HCAECs) were cultured at a density of 10,000 cells per well for four days in PrimaPure HCAEC Growth Medium with a powder concentration of 50 μg/mL. Cell viability was characterized using fluorescent dyes and live-dead microscopy techniques.

Results

Platinum is a preferred substitutional element for increasing radiopacity, so its partitioning behavior was determined. Using local electrode atom probe (LEAP) microanalysis, the Pt partitioning coefficient at 600°C was determined, $k_{Pt}^{B2/L21}=3.71$, and it was thus found that Pt negatively affects the misfit, strongly partitioning to the matrix phase rather than the precipitate phase. This is quite close to the measured Pt partitioning coefficient reasoned by Jung at 800°C [5]. Combining the results of the earlier study with this one, the partitioning behavior of the Ti-group elements (Zr and Hf) switch between 600° and 800°C, while the partitioning behaviors of the Ni-group elements (Pt and Pd) are constant at these temperatures. Thus, Zr and Hf both partition to the precipitate at 600°C, while Pd partitions to the precipitate at both 600° and 800°C. Pt partitions to the matrix at both 600° and 800°C. These results are summarized in Table I. Therefore, due to the design constraint of reducing misfit, alloy designs with solely Pt substitution were not further considered.

Table I. Partitioning coefficients for Zr, Hf, Pd, and Pt in the B2-$L2_1$ TiNi-based system [5]

$k_x^{B2/L21}$	600°C	800°C
Zr	0.75	1.35
Hf	0.87	2.17
Pd	0.60	0.64
Pt	3.71	3.71

(Ni,Pt)(Ti,Zr,Al) compositions were initially considered with both Pt for radiopacity and Zr for misfit, but Zr was found to stabilize Ni-rich precipitate phases and promotes the low-melting NiTiZr Laves phase leading to difficulty in high-temperature alloy manufacturing. A more efficient design utilizing Pd became the focus of this study.

Pd is identified as particularly advantageous as it stabilizes martensite, partitions to the Heusler phase at 600°C reducing misfit, improves radiopacity, and substitutes for Ni, which potentially improves biocompatibility. LEAP microanalysis of NiPdTiAl alloys revealed two-phase B2-$L2_1$ microstructures with a very Pd-rich $(Pd,Ni)_2TiAl$ Heusler phase. The composition tie-lines are plotted on a pseudo-ternary phase diagram in Fig. 6, where Ni and Pd are combined.

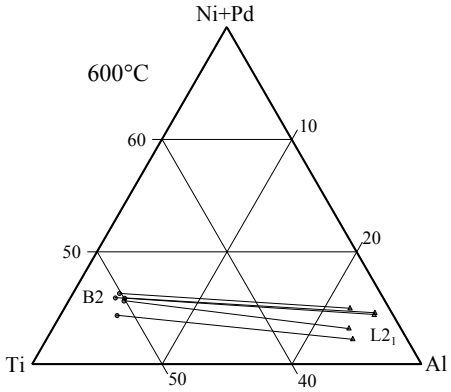

Figure 6. B2-$L2_1$ phase relations for NiPdTiAl system

For NiPdTiAl alloy designs, it is vital to model the transformation temperatures. In order to quantify the effect of Al on the A_f temperature, the transformation temperatures of NiTiAl alloys were measured using DSC. The presence of R-phase was observed in all of the alloys. It is well known that elements that suppress the martensitic transformation (i.e. Al, Fe) promote the R-phase and that the exothermic R-phase transformation remains stable while the other transformations shift toward lower temperatures with increased cycling due to accommodation slip. As an example, the first five DSC temperature cycles for a $Ti_{50}Ni_{47.5}Al_{2.5}$ alloy are shown in Figure 7.

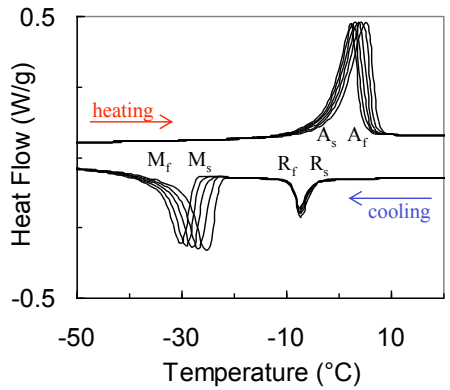

Figure 7. DSC transformation behavior of solution treated $Ti_{50}Ni_{47.5}Al_{2.5}$, indicating the presence of the R-phase

Eight NiTiAl buttons were tested giving the transformation temperatures listed in Table II. The plots in Figure 8 show the difference in A_f temperature depression depending on the sublattice of Al substitution.

Table II. Experimental DSC transformation temperatures for various NiTiAl alloys

Alloy	M_f	M_s	A_s	A_f	$H=A_f-M_s$
$Ni_{50}Ti_{49.5}Al_{0.5}$	-44	-38	-3	5	43
$Ni_{50}Ti_{49.75}Al_{0.25}$	-33	-28	19	31	59
$Ni_{50}Ti_{49.85}Al_{0.15}$	16	28	49	62	34
$Ni_{49.5}Ti_{49.5}Al_1$	9	24	57	63	39
$Ni_{49.25}Ti_{49.25}Al_{1.5}$	-35	-31	31	36	67
$Ni_{49}Ti_{50}Al_1$	35	42	67	72	30
$Ni_{47.5}Ti_{50}Al_{2.5}$	-30	-23	-1	7	30
$Ni_{50.5}Ti_{49}Al_{0.5}$	< -60	< -60	-52	-48	-

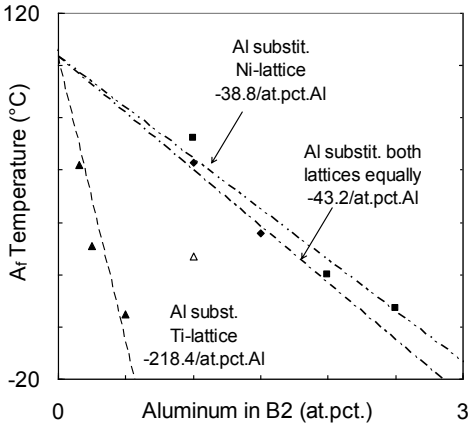

Figure 8. Austenite finish (A_f) temperature depression as a function of B2 Al content and Al substitution site

Once the effect of Al substitution on A_f temperature was quantified, a few button melts of NiPdTiAl alloys were tested to study the cross effects of Pd and Al on the A_f temperature. The transformation temperatures are listed in Table III. The A_f temperatures are plotted in Figure 9. Integrating ternary TiNiPd data from the literature, a Redlich-Kister polynomial model is fit to the quaternary system.

Table III. Experimental DSC transformation temperatures for various NiPdTiAl alloys

Nominal Composition (at.%)				Transf. Temperatures (°C)			
Ni	Pd	Ti	Al	M_f	M_s	A_s	A_f
30	20	49	1	51	53	70	74
25	25	49	1	124	138	140	147
25	25	47	3	-45	-37	-27	-10
23	27	47	3	8	10	29	37
20	30	47	3	97	107	114	123
14	36	46	4	103	106	123	134
17.5	32.5	46	4	62	65	84	95

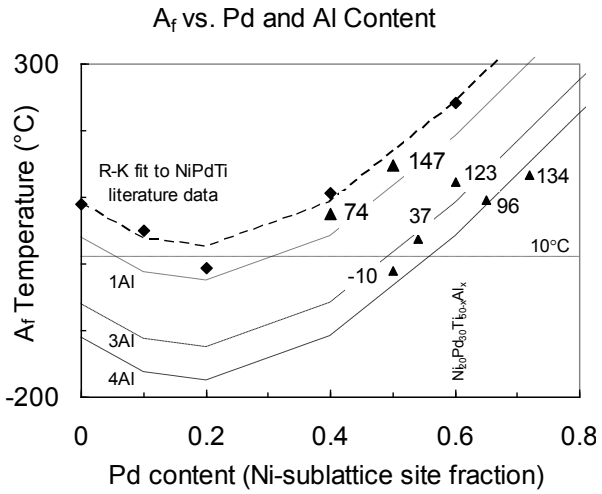

Figure 9. Austenite finish (A_f) temperature of solution treated NiPdTiAl alloys as a function of Al and Pd content

Building on our previous thorough study of isothermal precipitation in a $Ni_{50}Ti_{38}Zr_8Al_4$ alloy [8], the precipitate size of each NiPdTiAl alloy at one or two aging times (1, 5, 10, and 100 h) was measured. These precipitate are plotted in Figure 10 together with the data from the previous NiTiZrAl study. While the time constant for NiPdTiAl alloys is higher, Langer-Schwartz high-supersaturation precipitation behavior is still supported. While a 10 h aging treatment was required to produce an optimal precipitate size in NiTiZrAl alloys, experimental data predicts that only a 4 h aging treatment at 600°C is required to produce precipitates of the same 3.1 nm diameter for maximum strengthening.

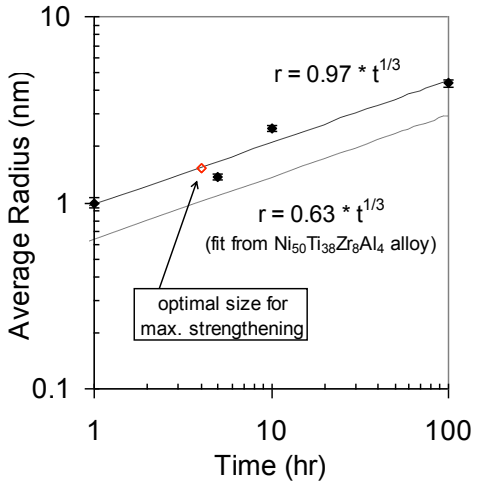

Figure 10. Modeling precipitate size versus aging time at 600°C in NiPdTiAl alloy

In order to demonstrate a proof-of-concept, transforming, precipitation-strengthened design, an $Ni_{14}Pd_{36}Ti_{46}Al_4$ alloy was arc-melted and tested. The DSC results following a solution treatment are shown in Figure 11. The DSC results and LEAP reconstruction following a 10 h aging are shown in Figure 12.

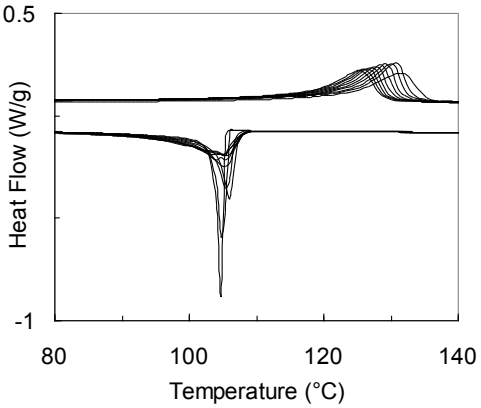

Figure 11. DSC results of $Ni_{14}Pd_{36}Ti_{46}Al_4$ solution treated at 950°C

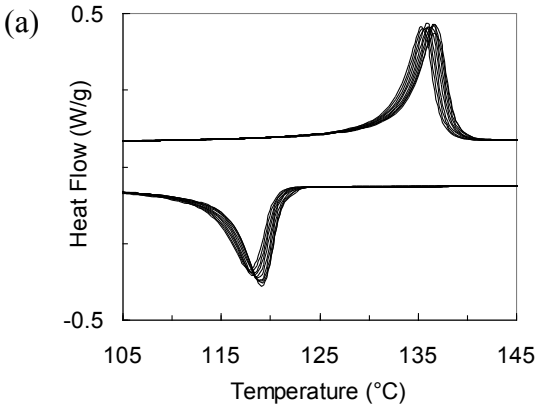

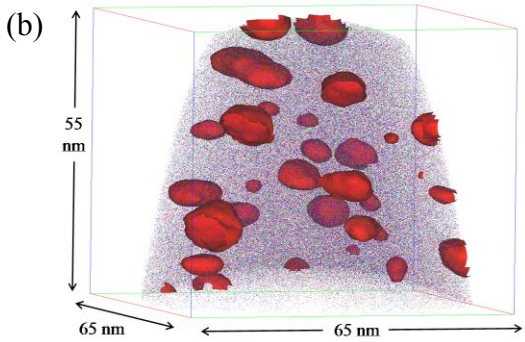

Figure 12. (a) DSC results and (b) atom probe reconstruction of $Ni_{14}Pd_{36}Ti_{46}Al_4$ aged at 600°C for 10 h

Once shape-memory transformation behavior was demonstrated in Heusler phase precipitation-strengthened alloys, martensite stability was fine tuned to design an alloy that would be superelastic at body temperature. The resulting design was the $Ni_{20}Pd_{30}Ti_{46}Al_4$ (at.%) alloy, which had an A_f temperature of 10°C, as demonstrated in the DSC curves of Figure 13. The exact composition of the arc-melted button is $Ni_{19.6}Pd_{29.7}Ti_{46.7}Al_{4.02}$, which was determined using an ICP-MS technique by Shiva Technologies, an Evans Analytical Group (Syracuse, NY). In addition to having an appropriate A_f temperature for endovascular stents, this precipitation-strengthened alloy demonstrated thermal cyclic stability; the transformation temperatures do not shift, but remain constant through 30 temperature cycles. The presence of the Heusler nanodispersion was verified using LEAP microanalysis. An atom probe reconstruction of $Ni_{20}Pd_{30}Ti_{46}Al_4$ with nearly optimized average precipitate size is shown in Figure 14.

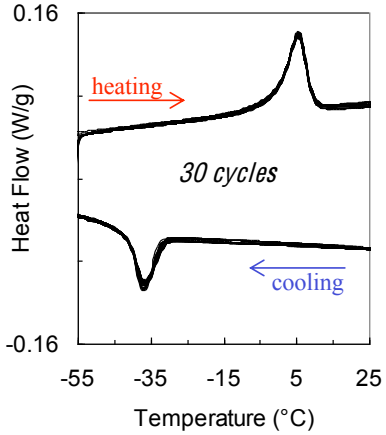

Figure 13. $Ni_{20}Pd_{30}Ti_{46}Al_4$ alloy aged at 600°C for 5 h (A_f = 10°C)

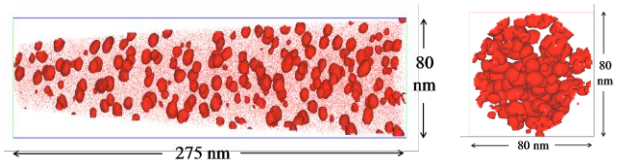

Figure 14. Atom probe reconstruction of $Ni_{20}Pd_{30}Ti_{46}Al_4$ alloy aged at 600°C for 5 h confirming the presence of Heusler phase precipitates (denoted with Al=12.5 at.% isoconcentration surfaces)

LEAP compositional analysis is utilized to calculate a low misfit, δ=0.71%, at 600°C. This is decreased from the -2.30% misfit found in ternary NiTiAl B2-$L2_1$ alloys.

The low-dose, long-time preliminary cytology study returned positive results demonstrating that $Ni_{20}Pd_{30}Ti_{46}Al_4$ is comparable to pure Ti and the control case. Ni powder served as the negative control and, as such, decreased cell viability. In this study, the TiNi alloy is an anomaly as it performs unusually poorly; however, the TiNi powder was not heated to enrich the surface with Ti prior to testing, which may account for its poor behavior in this study. These results are summarized in Figure 15.

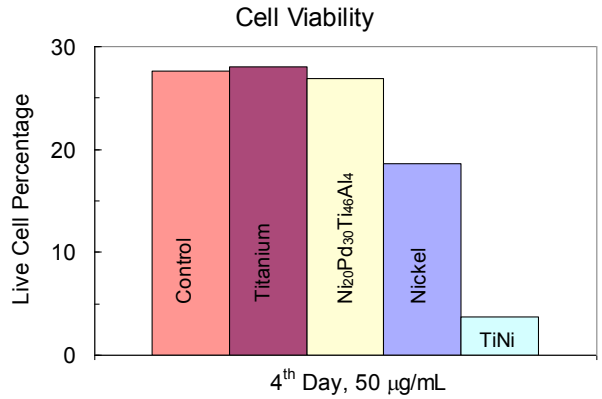

Figure 15. Cell viability at the end of a four-day cytology study comparing $Ni_{20}Pd_{30}Ti_{46}Al_4$ to a control, Ti (a positive control), Ni (a negative control), and binary TiNi

Radiopacity was quantitatively modeled using mass attenuation coefficients (μ/ρ), which can be used to calculate the x-ray transmission according to the following equation:

$$I / I_0 = \exp (- (\mu/\rho) \times \rho \times x)$$

where I_0 is the incident x-ray intensity, I is the transmitted intensity, ρ is the alloy density, and x is the material thickness. Stent delivery and deployment is typically performed at a fluoroscopy operating energy of 90 keV. While fluoroscopy utilizes a polychromatic beam, the mass attenuation is modeled at a singular energy of 30 keV because the largest number of x-rays have 1/3 the operating energy and this value is greater than the Pd K-edge energy. Assuming a small medical stent strut thickness of 40 μm, radiopacity improvements were calculated and compared to binary TiNi, as listed in Table IV. The $Ni_{20}Pd_{30}Ti_{46}Al_4$ alloy radiopacity is greatly enhanced.

Table IV. Comparison of radiopacity at 30 keV

Compound	μ/ρ @ 30 keV	Absorption $(1-I/I_0)$	Radiopacity Improvement
TiNi	7.93	18.6%	0.0%
SS-316	9.11	25.1%	34.9%
$Ni_{20}Pd_{30}Ti_{46}Al_4$	20.00	45.0%	141.9%

Qualitative x-ray fluoroscopy validation was performed to confirm the radiopacity improvement of the alloy. Radiopaque materials have darker contrast in fluoroscopy images, which is the opposite of radiograph images. The fluoroscopy image shown in Figure 16 demonstrates the improvement in $Ni_{20}Pd_{30}Ti_{46}Al_4$ over both TiNi and SS-316, all at 127 μm thickness. The Al wedge varies in thickness from 0-2.5 cm over a 12 cm length. $Ni_{20}Pd_{30}Ti_{46}Al_4$ has an Al-equivalent thickness of 5.7 mm while TiNi and SS-316 have approximate Al-equivalent thicknesses of 0.5 mm.

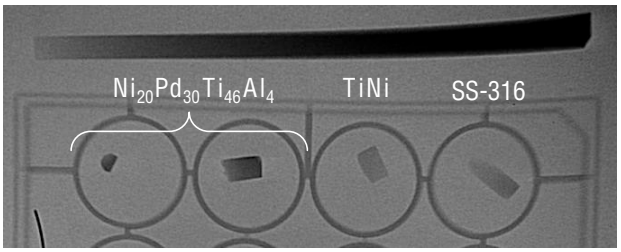

Figure 16. X-ray fluoroscopy image of 127 μm samples showing improvement in radiopacity of $Ni_{20}Pd_{30}Ti_{46}Al_4$ alloy over both TiNi and SS-316

Compression cylinders machined from a second $Ni_{20}Pd_{30}Ti_{46}Al_4$ arc melted button were tested using an Instron machine at a temperature of A_f + 25°. While the nominal composition was the same, this second button had an A_f temperature of 66°C, suggesting some composition variation, which was confirmed with ICP-MS testing. The composition of this second button from which compression samples were machined was $Ni_{18.8}Pd_{30.4}Ti_{47.1}Al_{3.67}$. The A_f temperature of binary TiNi is often set at 10-15°C for stent applications, while it performs at body temperature (37°C), approximately 25° higher. Therefore, for these compression samples with an A_f=66°C, the test temperature was chosen to be 90°C. The compression test results are shown in Figure 17. The initial superelastic loops were repeated six times before increasing the strain. For each consecutive strain tested, the superelastic loops are very stable over 4-6 repeated loops. The fracture stresses for the solution treated and aged specimens were 2.96 and 2.74 GPa [19], respectively, while the strains at failure were 34% and 27%, respectively. To be certain that this transforming alloy was also precipitation-strengthened, aluminide precipitation was confirmed using atom probe microanalysis.

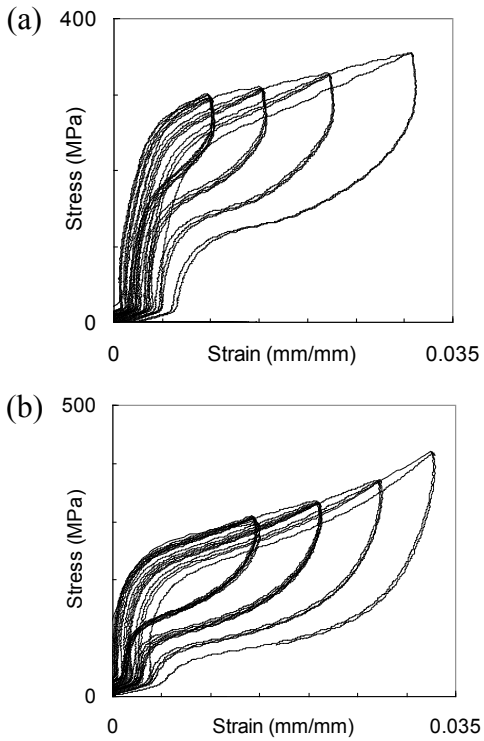

Figure 17. Compression testing at $A_f + 25°$ of $Ni_{20}Pd_{30}Ti_{46}Al_4$ (a) solution treated and (b) aged (600°C, 5h)

Conclusions

Comparison of Heusler phase precipitation-strengthened NiPdTiAl alloys to binary TiNi demonstrates greatly enhanced stability under temperature cycling (Figure 18) and mechanical superelastic cycling (Figure 19). This cyclic stability is a strong indication of improved fatigue life in this class of alloys.

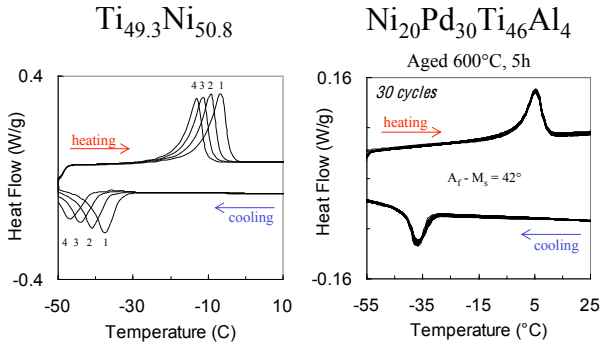

Figure 18. Thermal cyclic stability comparison between binary TiNi and aged $Ni_{20}Pd_{30}Ti_{46}Al_4$ alloy

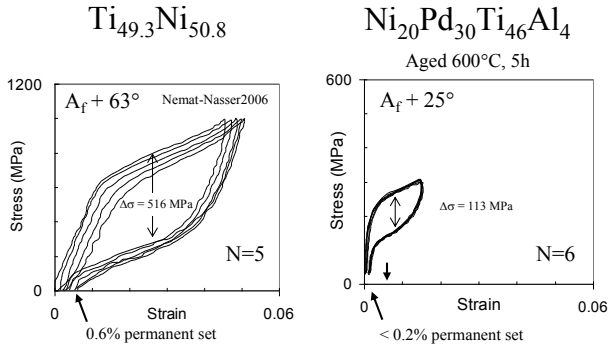

Figure 19. Mechanical cyclic stability comparison between binary TiNi [20] and aged $Ni_{20}Pd_{30}Ti_{46}Al_4$ alloy tested at $A_f + 25°$

In Figure 18, the transformation temperatures of a binary TiNi alloy shift by 10° during the first four cycles, while the aged $Ni_{20}Pd_{30}Ti_{46}Al_4$ alloy remains stable through the 30 cycles tested.

Figure 19 compares the first five cycles from a compression test of annealed binary TiNi [20] with the first six cycles from a compression test of $Ni_{20}Pd_{30}Ti_{46}Al_4$. The permanent strain is decreased from 0.6% in the binary alloy to less than 0.2% in $Ni_{20}Pd_{30}Ti_{46}Al_4$. The stress hysteresis, $\Delta\sigma$, is greatly decreased in the designed precipitation-strengthened alloy from approximately 516 MPa to 113 MPa. There is a somewhat smaller transformation strain in the Pd-containing alloy compared to binary TiNi, as observed in other TiNiPd alloys in association with B19 martensite [21].

The direct comparison of Heusler phase precipitation-strengthened alloys to binary TiNi demonstrates greatly enhanced stability under temperature cycling and mechanical superelastic cycling. While these experiments indicate that the alloy fatigue life should be enhanced through the minimization of accommodation slip, further fatigue testing is necessary to examine a full S-N curve of this material to fully demonstrate the improvement in cyclic fatigue life. The nanoscale precipitation-strengthened, superelastic alloy should meet the performance requirements of future medical endovascular stent applications.

Acknowledgements

Financial support from the U.S. Air Force Office of Scientific Research (AFOSR) through a National Defense Science and Engineering Grant (NDSEG) Fellowship is gratefully acknowledged, as is financial support from Medtronic, Inc. Atom probe microanalysis was performed at the Northwestern University Center for Atom Probe Tomography (NUCAPT). Research Professor Dieter Isheim is kindly thanked for managing NUCAPT and providing technical advice. Dr. Mark Eskandari of Northwestern Memorial Hospital is kindly thanked for providing access to an x-ray fluoroscope.

References

1. Miyazaki, S., Igo, T., and Otsuka, K. Acta Metall. 34 (10):2045-2051, 1986

2. Olson, G.B. and Owen, W.S. Proc. ICOMAT-75, First JIM International Symposium, May 1976, p. 105-110

3. Adler, P.H., Allen, J., Lessar, J., and Francis, R. Journal of ASTM International, 4 (7):1-16, 2007

4. Zadno, G.R., Yu, W., and Duerig, T.W. Raychem Corporation, internal publication, 1989

5. Jung, J., Ghosh, G., and Olson, G.B. Acta Materialia 51:6341-6357, 2003

6. Riepe, G.C., Heintz, E., Kaiser, N., Chakfe, M., Morlock, M., Delling, M., and Imig, H. European Journal of Vascular and Endovascular Surgery, 24:117-122, 2002

7. Allie, D.E., Hebert, C.J., and Walker, C.M. Endovascular Today, July/August 2004, p.22-34

8. Bender, M.D. and Olson, G.B. ICOMAT proceedings, 2008

9. Ito, A., Okazaki, Y., Tateishi, T., and Ito, Y. Journal of Vascular Surgery, 37 (1):16-26, 1995

10. Shroeder, H.A., Mitchener, M., and Nason, A.P. J. Nutrition, 100:59-68, 1970

11. Ganrot, P.O. Environ. Health Perspect., 65:363-441, 1986

12. Ghosh, S., Sharma A., and Talukder, G. Biol. Trace Elem. Res., 35:247-271, 1992

13. Laing, P.G., Ferguson, A.B., and Hodge, E.S. J. of Biomedical Materials Research, 1:135-149, 1967

14. Bessing, C. and Kallus, T. Acta Ordontol. Scand., 45:247-255, 1987

15. Aberer, W., Holub, H., Strohal, R. And Slavicek, R. Contact Dermatitis, 28:163-165, 1993

16. Rocher, P., Medawar, L.E., Hornez, J.C., Traisnel, M., Breme, J., and Hildebrand, H.F. European Cells and Materials, 9:23-24, 2005

17. Azman, A., Hsieh, C., Hughes, G., Jiang, T., and Lin, A. “Stentalloy 2008,” Final Project Report of Materials Design course, Northwestern University, 2008

18. Wang, C., Wells, H., Hemphill, Z., and Suresh, S. “SmartStent,” Final Project Report of Engineering Design and Communication course, Northwestern University, 2008

19. Bender, M.D. PhD thesis, Northwestern University, Evanston, IL, 2008

20. Nemat-Nasser, S. and Guo, W.-G. Mechanics of Materials 38:463-373, 2006

21. Noebe, R., Biles, T. and Padula, S.A. Advanced Structural Materials: Properties, Design Optimization, and Applications. CRC Press, 2006, p.145-181